LAWRENCE
LIVERMORE
NATIONAL
LABORATORY

LLNL-JRNL-411390

Characterization of Heat-Wave Propagation through Laser-Driven Ti-Doped Underdense Plasma

M. Tanabe, H. Nishimura, N. Ohnishi, K. B. Fournier, S. Fujioka, A. Iwamae, S. B. Hansen, K. Nagai, F. Girard, M. Primout, B. Villette, D. Brebion, K. Mima

March 19, 2009

High Energy Density Physics

Disclaimer

Characterization of heat-wave propagation through laser-driven Ti-doped underdense plasma

Minoru Tanabe[*,a], Hiroaki Nishimura[a], Naofumi Ohnishi[b], Kevin B. Fournier[c], Shinsuke Fujioka[a], Atsushi Iwamae[d,1], Stephanie B. Hansen[c,2], Keiji Nagai[a], Frederic Girard[e], Michel Primout[e], Bruno Villette[e], Didier Brebion[e], Kunioki Mima[a]

[a] *Institute of Laser Engineering, Osaka University, 2-6 Yamada-Oka, Suita, Osaka 565-0871, Japan*
[b] *Department of Aerospace Engineering, Tohoku University 6-6-01 Aramaki-Aza-Aoba, Aoba-ku, Sendai 980-8579, Japan*
[c] *Lawrence Livermore National Laboratory, P.O. Box 808, L-473, Livermore, California 94550, USA*
[d] *Department of Mechanical Engineering and Science, Kyoto University, Kyoto 606-8501, Japan*
[e] *Commissariat a l' Energie Atomique, DAM-Ile-de-France, Bruyeres-le-Chatel, 91297 Arpajon, Cedex, France*

Abstract

The propagation of a laser-driven heat-wave into a Ti-doped aerogel target was investigated. The temporal evolution of the electron temperature was derived by means of Ti K-shell x-ray spectroscopy, and compared with two-dimensional radiation hydrodynamic simulations. Reasonable agreement was obtained in the early stage of the heat-wave propagation. In the later phase, laser absorption, the propagation of the heat wave, and hydrodynamic motion interact in a complex manner, and the plasma is mostly re-heated by collision

[*]Corresponding author. Tel.: +81 6 6879 8777; fax: +81 6 6877 4799.
Email address: mtanabe@ile.osaka-u.ac.jp (Minoru Tanabe)
[1]Present address: Japan Atomic Energy Agency
[2]Permanent address: Sandia National Laboratories

and stagnation at the target central axis.

Key words: Laser-produced plasma; X-ray spectroscopy; Plasma diagnostics; X-ray generation

PACS: 52.38.Ph; 52.50.Jm; 52.70.La; 52.59.Px

---

1. Introduction

Efficient multi-keV x-ray sources are necessary for backlighters in radiograph of dense matters in high-energy-density physics and inertial-confinement-fusion experiments [1, 2]. Because the densities of these objects are high, the x-ray sources need to have high conversion efficiency (CE), higher photon energies, and could be spatially uniform. Multi-keV x-ray sources from laser-produced plasma have been investigated with various kinds of targets [3, 4, 5, 6, 7, 8, 9, 10, 11, 12, 13, 14]. In thick solid targets [3, 4, 5], CEs were only fractions of a percent for multi-keV x-ray photon energies and show a strong logarithmic decrease with increasing photon energy [11]. The effective volume of plasma for multi-keV x-ray generation is very much localized due to steep gradients in density and temperature. A radiation-hydrodynamics code, ILESTA-1D (Ref. [15]) predicts that the typical scale length is approximately 100 μm with a laser pulse of 351 nm in wavelength and 1.0 ns in duration at 1×10^{15} W/cm^2. In contrast, low-density targets such as gases [6, 7, 8], high-Z doped aerogels [9], or nano-structured materials [10], have electron densities that can be less than the critical density for a frequency doubled or tripled laser wavelength even at full ionization. Thus, laser absorption occurs predominately by inverse bremsstrahlung and the targets are heated supersonically and volumetrically in prior to hydrodynamic

expansion [12, 16]. The supersonic and volumetric heating mechanisms of the target are known as a new pathway for efficient multi-keV x-ray generation [6, 9, 10, 13, 14]. Recent experiments with underdense targets show higher CE numbers than with solid targets [6, 9, 10]. In order to clarify the optimal conditions of efficient multi-keV x-ray generation, not only is development of new target materials needed but also understanding energy transport in these plasmas is important.

Several investigations have been performed to observe the heat-wave propagation into underdense plasmas and to diagnose profiles of electron temperature and density [7, 12, 14, 17]. Agar foam and aerogel (4–9 mg/cm^3) targets were driven with laser intensities in the range of 10^{14}–10^{16} W/cm^2 [17]. The heat-wave front observed with a time-resolved x-ray imager was shown to be slower than the theoretical predictions. This discrepancy between the experiments and the simulations is attributed to strong scattering of the drive laser, anomalous absorption, and/or hydrodynamic compression above the critical density. The closest condition to our study in terms of target material is that reported in the work of Constantin *et al* [12]. Comparisons between experiments and model predictions suggested that nonlocal heat transport effects may contribute to the attenuation of the heat-wave propagation for laser intensities at or above few times 10^{15} W/cm^2. Moreover, time- and space-averaged electron temperatures inferred from the x-ray spectra were 2–3 keV.

The novelty in our work is that the temporal evolution of electron temperature in an underdense plasma is diagnosed at a laser intensity of several times 10^{14} W/cm^2, and experimental electron temperatures are compared

in detail with those simulated with the two-dimensional (2D) radiation-hydrodynamic simulation, RAICHO (see Ref. [18]).

2. Experimental setup

Experiments were carried out the GEKKO XII-HIPER (High Intensity Plasma Experimental Research) laser facility in the Institute of Laser Engineering, Osaka University [19]. Nine laser beams of frequency-tripled (351 nm) light with two-dimensional smoothing by spectral dispersion [20] were used. The laser pulse waveform was a bell-like shape with a 2.5 ns full-width-half-maximum. The beams were bundled into a cone with a half angle of 9.4°, corresponding to an F/3 focusing. All beams were focused at 1130 μm in front of the target surface. The laser intensity on the target surface was 4–5$\times$10 ^{14} W/cm^2.

The targets used in this study were low-density silica (SiO_2) aerogels doped with 3% titanium by atomic number at initial density of 3.2 mg/cm^3 [9]. Assuming full ionization of the aerogel, the electron density was equal to 0.1 times the critical density for a laser wavelength of 351 nm. The aerogel was enclosed in an 75-μm-thick beryllium cylinder of 1.94 mm in length and 1 mm in outer diameter.

To measure Ti K-shell x-ray emission from the targets, four main x-ray diagnostics were installed as shown in Fig. 1. The primary x-ray diagnostics was a flat rubidium acid phthalate (RbAP) crystal spectrometer coupled to an x-ray streak camera, (x-ray streak spectrograph: XSS). It was fielded at a side-on view of the cylinder target. Temporal resolution was 56 ps and spectral resolution $E/\Delta E$ (E: photon energy) was 200. The spectral window of

observation was from 4.6 to 5.8 keV, which includes the following Ti K-shell resonance lines: $\mathrm{He}_\alpha(1s^2 - 1s2p)$, $\mathrm{Ly}_\alpha(1s - 2p)$, and $\mathrm{He}_\beta(1s^2 - 1s3p)$. To restrict the observable region and also to attain high spectral resolution, a 100-μm-width slit was set at 1.5 mm away from the target in the line of sight of the XSS. The substrate of the slit was a 50-μm-thick tantalum foil. The observable regions were chosen to be 70-170 μm and 420-520 μm behind the irradiated target surface by changing the position of the slit along the target cylinder axis. An x-ray streak camera (XSC) was installed perpendicular to the cylinder axis in order to observe heat-wave front propagation into the target. A 20 μm diameter pinhole imager was used and the image magnification was 8.7. A 100-μm-thick beryllium debris shield was set in front of the imager and a K-edge absorption filter of 5-μm-thick titanium foil was used to detect only the photon energy from 4.7 to 4.9 keV. A 700-μm-width copper iodide slit was aligned in parallel to the cylinder axis to observe only the region close to the target cylinder axis. Spatial resolution was 23 μm and temporal resolution was about 100 ps. Photometrically calibrated x-ray diodes were installed on the laser-illumination side to measure conversion efficiency into x rays in the range of 4–6 keV.

3. Experimental results

Figure 2 shows time-resolved x-ray spectra for the region of 70-170 μm behind the target surface. Corresponding intensity lineouts at 0.98 ns, 2.27 ns, and 3.35 ns are shown in Fig. 3. The Ti-He_α, He_β resonance, and lithiumlike satellite lines are identified. The Ly_α emission is weak because the target was not heated to a high enough temperature. The intercombination

transition and dielectronic satellite transitions (Li-like satellites) are partly overlapped with the Ti-He$_\alpha$ line due to the limited spectral resolution of the XSS. Similar spectra were obtained for the region 420-520 μm behind the target surface. To derive temporal evolution of electron temperature from the observed spectra, an atomic kinetics code, FLYCHK [21] was used. Line intensity ratios of the Ti-He$_\alpha$ to the Li-like satellites, as well as the ratio of the He$_\alpha$ line to He$_\beta$ line, were adopted as diagnostics. The electron density was assumed to be 9.0×10^{20} cm^{-3}. Spectra calculated with FLYCHK were convolved with the instrumental spectral resolution. The synthetic spectra for best-fit electron temperatures are also presented in Fig. 3. In the FLYCHK code, the dielectronic satellite transitions seen in the red wing of the He$_\beta$ are not included. Given that, the synthesized spectra agree quite well with the observed spectra for the electron temperatures shown in the figure. Electron temperatures at other times for the two observable regions varied in the range from 600 to 1100 eV. Temporal evolution of electron temperature and comparison with the simulation results are discussed in detail in Sec. 5.

Figure 4 shows a typical streaked x-ray image. Since x-ray emission arises from high temperature region dominated by the Ti-He$_\alpha$ emission, the image indicates that heat wave propagates from the target surface toward the other side of the target. The target was illuminated from the left-hand side. The time origin was adjusted to coincide with the RAICHO simulation results. Trajectory of the heat-wave front position at a particular time was defined as the $1/e$ rising edge in x-ray intensity moving along the axial direction. The velocity of the heat-wave propagation into the target was measured to be 4.8

$\times 10^7$ cm/s.

4. Hydrodynamics simulations

To simulate the experimental results, we used RAICHO [18], a 2D, Eulerian radiation-hydrodynamics code with cylindrical axis-symmetric geometry (radial direction and axial direction). The simulation included experimental laser energy, laser spot, and pulse shape. Two-dimensional ray-tracing techniques were used to track the laser propagation into the target. Laser energy was deposited by inverse bremsstrahlung. The thermal electron conduction was treated with the classical Spitzer-Härm formula [22] with a flux limiter $f = 0.1$.

The main results of the RAICHO simulations are temporal and spatial dependence of the electron density, electron temperature, laser energy deposition, and laser ray-racing. Figure 5 shows the time- and space-resolved electron density and temperature mappings calculated with RAICHO at 2.00, 2.25, 2.50, 2.75, and 3.00 ns. Also, figure 6 shows time- and space-resolved laser rate-tracing and laser heating rate calculated with RAICHO at the same times. For all images, the target is irradiated from the left-hand side. To compare with the experimental x-ray streaked image shown in Fig. 4, temporal evolution of spatial electron temperature profile along the center of the cylinder axis calculated with RAICHO is shown in Fig. 7. The RAICHO simulation replicates well the experiment until the heat-wave reaches the cylinder end opposite the laser irradiation side. As shown in Fig. 8, the trajectory of the measured heat-wave front is in particularly good agreement with the position of the 900 eV contour in the simulation. However,

in the later phase, heating of the target is substantially affected by complicated interplay among laser light penetration, heat-wave propagation, and hydrodynamic motion shown in Figs. 5-7.

In the early phase of the target irradiation, the aerogel is partially ionized by the laser, and the rest of the laser energy is predominantly absorbed by inverse bremsstrahlung. Then, an ionization wave is created at the absorbed region [16]. It further propagates into the aerogel (see Figs. 5 (a) and (b)). After the heat wave reaches the other side of the target at around 2.0 ns, the high temperature region moves backward toward the laser-incident side as time advances. This result suggests that a part of the laser light reflected by the plasma expanded from the cylinder wall is focused at the cylinder center that this point moves backward to the laser incident side (see Figs. 6 (a), (b), (c), and (d)). Finally, the plasma expanding from the cylinder wall stagnates at the center of the cylinder near the laser-irradiated front side. As a consequence, the electron temperature and density at the front side of the target increase as shown in Figs. 5 (c), (d), (e), and Fig. 7.

5. Analysis of electron temperature history

As noted above, the interactions between the laser and underdense plasma are complicated and generally are not amenable to simple analysis. However, the experimental results and the RAICHO simulations provide some indications of the interaction of physical processes. Electron temperature is a particularly important quantity because it can be directly compared with the simulation results to help us to understand heating processes in an underdense plasma. We focused on the phenomena occurring near the front

side of the target.

In order to compare the experimental electron temperature with the simulation results, the electron temperature calculated with RAICHO was post-processed by integration along the line of sight over all plasma elements and weighted by emissivity of each plasma element. Therefore, volume-averaged temperature must be calculated using the electron temperature based on the RAICHO results. Moreover, emissivity of each plasma element must be taken into consideration as a weighting factor. Figure 9 shows a flow diagram of the post-processing process. First, the time-dependent x-ray emissivities for each plasma element were calculated by inputting electron temperatures and densities calculated from RAICHO into the FLYCHK code. Here, the character i represents an element number counted along to the radial direction of the cylinder. In the RAICHO simulation, the element size along the radial direction was chosen to be 10 μm. Then, the sum of emissivity of the time-dependent spectra in the range from 4 to 6 keV was calculated. Finally, the time-dependent, volume-averaged electron temperatures including emissivity weighting factors were calculated with the equation given in Fig. 9. Figure 10 shows the comparison between the diagnosed time-evolution of electron temperature (dots) and the post-processed electron temperature (lines) for the two different observable regions. As discussed in Sec. 4, the temperature increases rapidly as the underdense target is heated by the laser. Then, the electron temperature decreases slightly as the high temperature region moves back the other side of the cylinder, and finally the underdense plasma is re-heated by the plasma stagnation at the cylinder axis. This scenario agrees reasonably well with the measured data in terms of the absolute values of

the temperatures and their time history.

The x-ray conversion efficiency, defined as the ratio of the total x-ray output in the 4–6 keV band into 4π solid angle to the incident laser energy, was 0.34±0.4%. In comparison with the identical target reported in Ref. [12], this CE is quite low. The reason is due to the higher laser intensity (1.7×10^{15} and 3.4×10^{15} W/cm^2 for the case in Ref. [12]) and different laser focusing conditions. The FLYCHK code predicts that plasma with an electron temperature of 2.0–2.5 keV optimally generates Ti K-shell x-ray radiation (4–6 keV). The inferred electron temperatures in the present study are lower than the optimal temperatures. For a given laser focusing condition, higher electron temperatures can be obtained by utilizable plasma confinement in an enclosure and energy recovery by hydrodynamic collision.

6. Conclusion

The temporal evolution of electron temperatures in low-density laser-heated aerogel plasmas have been studied. Under the experimental conditions, electron temperatures range from 600 to 1100 eV at the front side of the target. Analysis of electron temperatures from the RAICHO simulation post-processed with FLYCHK has shown that plasma re-heating occurs due to the plasma stagnation on the cylindrical axis of the target following radial compression. We conclude that laser absorption, heat transport, and hydrodynamics in underdense plasma are all of relevance for benchmarking radiation-hydrodynamics codes and for development of efficient x-ray sources.

Acknowledgments

This work was performed under the auspices of the U.S. Department of Energy by Lawrence Livermore National Laboratory under Contract DE-AC52-07NA27344, the Ministry of Education, Cultures, Sports, Science and Technology of Japan project "Advanced Diagnostics for Burning Plasma (code 442) "Temperature and density mapping of imploded burning plasma with monochromatic x-ray imaging (code 20026005), and JSPS-CAS Core-University Program in the field of "Plasma and Nuclear Fusion".

References

[1] J. Nuckolls, L. Wood, A. Thiessen, et al., Nature (London) **239**, 139 (1972).

[2] R. Kodama, H. Shiraga, K. Shigemori, et al., Nature **418**, 934 (2002).

[3] D. W. Phillion and C. J. Hailey, Phys. Rev. A **34**, 4886 (1996).

[4] J. Workman and G. A. Kyrala, Rev. Sci. Instrum. **72**, 678 (2001).

[5] B. Yaakobi, P. Bourke, Y. Conturie, et al., Opt. Commun. **38**, 196 (1981).

[6] C. A. Back, J. Grun, C. Decker, et al., Phys. Rev. Lett. **87**, 275003 (2001).

[7] C. A. Back, J. Davis, J. Grun, et al. Phys. Plasmas **10**, 2047 (2002).

[8] K. B. Fournier, C. Constantin, C. A. Back, et al., J. Quant. Spectrosc. Radiat. Transf. **99**, 168 (2006).

[9] K. B. Fournier, C. Constantin, J. Poco, et al. Phys. Rev. Lett. **92**, 165005 (2004).

[10] M. Tanabe, H. Nishimura, S. Fujioka, et al., Appl. Phys. Lett. **93**, 051505 (2008).

[11] R. Kauffman, *Handbook of Plasma Physics* (Elsevier Science, 1991), chap. 3, p. 111.

[12] C. Constantin, C. A. Back, K. B. Fournier, et al. Phys. Plasmas **12**, 063104 (2005).

[13] F. Girard, J. P. Jadaud, M. Naudy, et al. Phys. Plasmas 12 **12**, 092705 (2005).

[14] D. Babonneau, M. Primout, F. Girard, et al., Phys. Plasmas **15**, 092702 (2008).

[15] H. Takabe, M. Yamanaka, K. Mima, et al. Phys. Fluids **31**, 2884 (1988).

[16] J. Denavit and D. W. Phillion, Phys. Plasmas **1**, 1971 (1994).

[17] J. A. Koch, K. G. Estabrook, J. D. Bauer, et al., Phys. Plasmas **2**, 3820 (1995).

[18] N. Ohnishi, M. Nishikino, and A. Sasaki, J. Phys. IV **133**, 1193 (2006).

[19] N. Miyanaga, M. Nakatsuka, H. Azechi, et al., in *The proceedings of the 18th International Conference on Fusion Energy* (IAEA, Sorrento, Italy, 2001), IAEA-CN-77.

[20] S. Skupsky, R. W. Short, T. Kessler, et al. J. Appl. Phys. **66**, 3456 (1989).

[21] H. K. Chung, M. H. Chen, W. L. Morgan, et al. High Energy Density Phys. **1**, 3 (2005).

[22] L. Spitzer and R. Harm, Phys. Rev. **89**, 977 (1953).

List of figure captions

FIG.1 Experimental setup showing layout of laser beams and x-ray diagnostic instruments. A slit was set at 1.5 mm in distance from the target surface to restrict the observable region.

FIG.2 Time-resolved Ti K-shell spectra measured with the x-ray streak spectrograph for the region of 70-170 μm behind the irradiated target's surface. The Ti-He$_\alpha$ and He$_\beta$ resonance lines and lithiumlike satellite lines are identified. The Ly$_\alpha$ emission is hardly seen.

FIG.3 Temporal variations of the observed spectra (solid lines) derived from the data shown in Fig. 2 at (a) 0.98, (b) 2.27, and (c) 3.35 ns. Spectra calculated with the FLYCHK code (dashed lines) are shown for comparison assuming the electron density of 9.0×10^{20} cm^{-3}.

FIG.4 Experimental x-ray streaked image. Laser beams are incident on the target from the left-hand side.

FIG.5 Time- and space-resolved electron densities and electron temperatures calculated with RAICHO at (a) 2.00, (b) 2.25, (c) 2.50, (d) 2.75, and (e) 3.00 ns. For all images, the upper and lower images show electron density in cm^{-3} and electron temperature in eV, respectively. Spatial origin is

the cross-over-point of the cylinder axis and the cylinder circle center. Laser beams are incident from the left-hand side.

FIG.6 Time- and space-resolved laser ray-tracing and heating rate calculated with RAICHO at (a) 2.00, (b) 2.25, (c) 2.50, (d) 2.75, and (e) 3.00 ns. For all images, the upper and lower images show ray-tracing and heating rate in W/cm^3, respectively. Laser beams are incident from the left-hand side.

FIG.7 Temporal evolution of electron temperature along the center of the cylinder axis calculated with RAICHO. Laser beams are incident from the left-hand side.

FIG.8 Comparison between the experimental heat-wave front (dots) and the calculated electron temperature front defined at electron temperature of 900 eV.

FIG.9 Flow diagram of the post-processing for the time-dependent, emissivity-weighted and volume-averaged electron temperature derived from RAICHO simulation and FLYCHK calculation.

FIG.10 Temporal evolution of electron temperatures inferred from the spectra (dots) and the emissivity-weighted and volume-averaged electron temperature (lines) at the region of (a) 70-170 μm and (b) 420-520 μm.

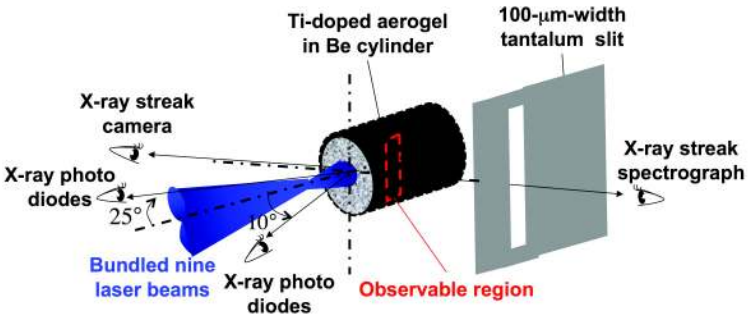

Figure 1: M. Tanabe et al., submitted to High Energy Density Physics

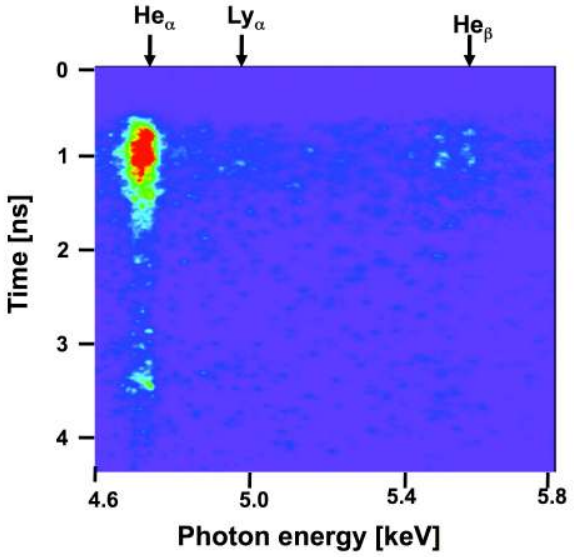

Figure 2: M. Tanabe et al., submitted to High Energy Density Physics

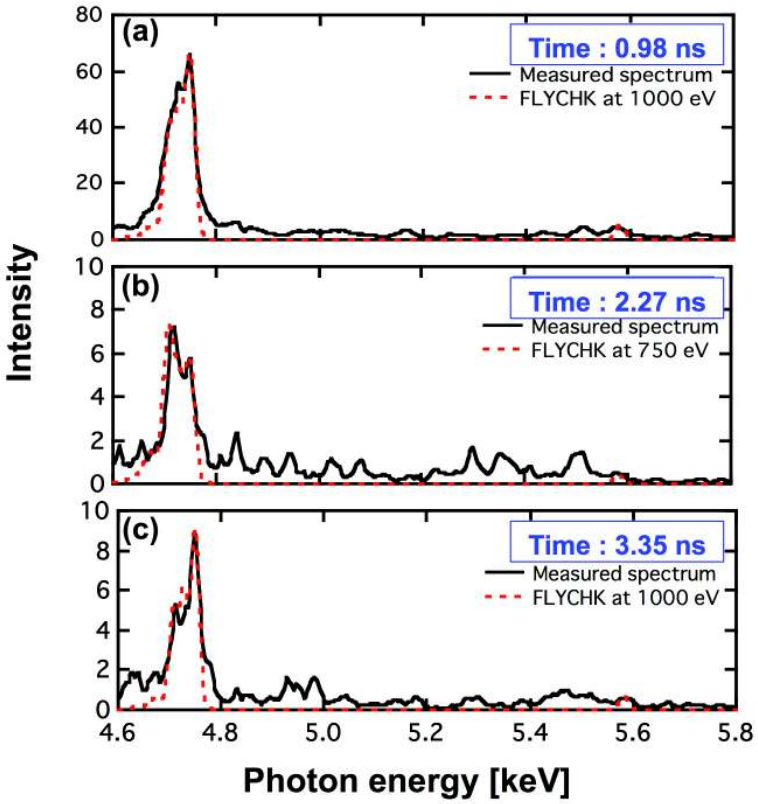

Figure 3: M. Tanabe et al., submitted to High Energy Density Physics

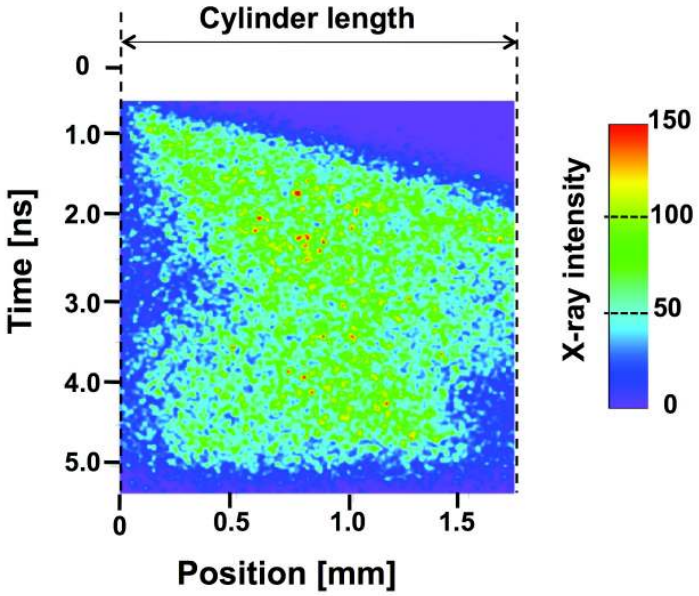

Figure 4: M. Tanabe et al., submitted to High Energy Density Physics

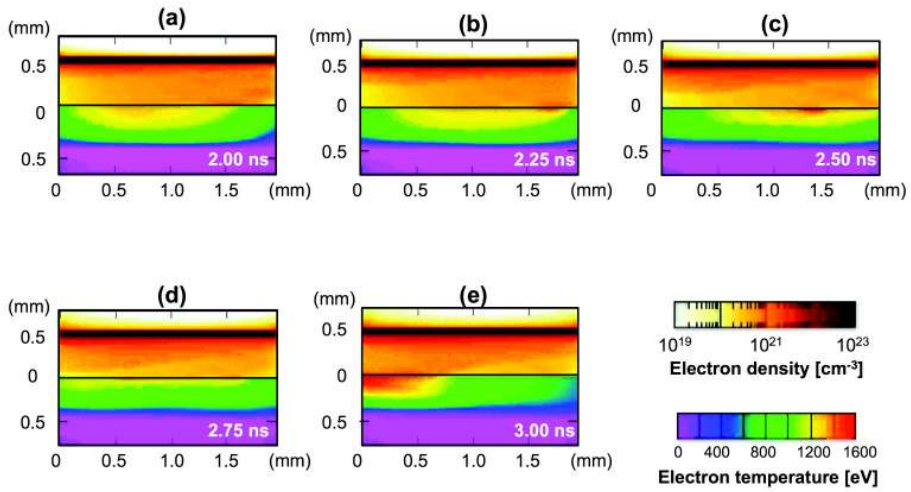

Figure 5: M. Tanabe et al., submitted to High Energy Density Physics

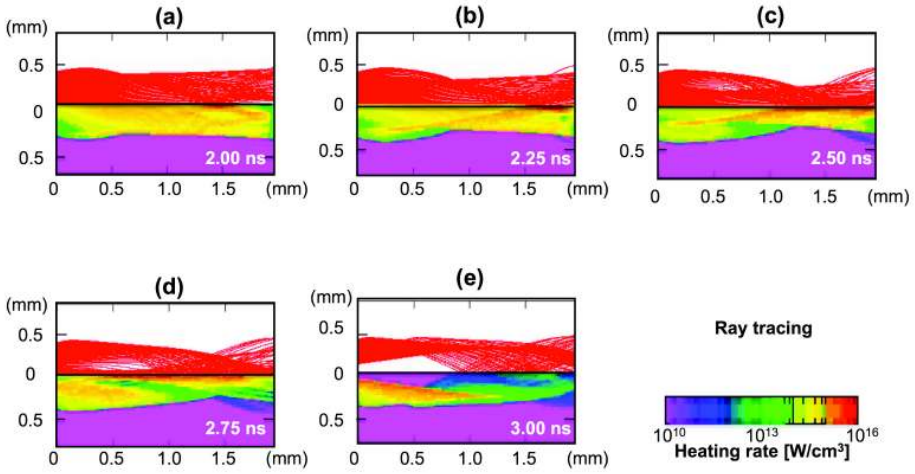

Figure 6: M. Tanabe et al., submitted to High Energy Density Physics

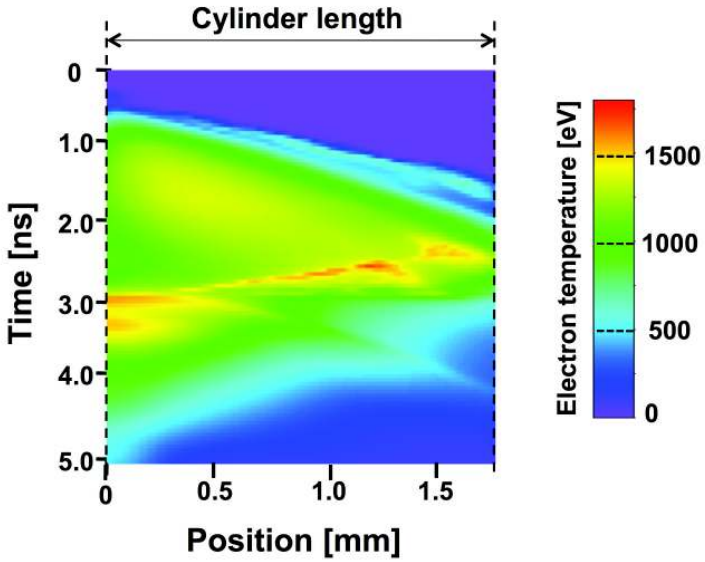

Figure 7: M. Tanabe et al., submitted to High Energy Density Physics

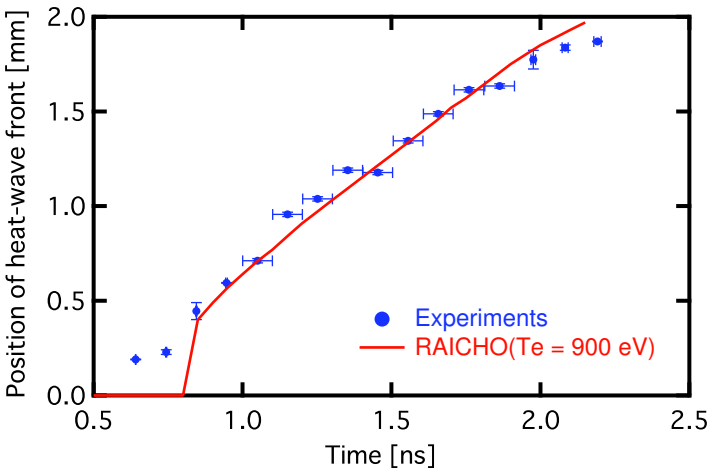

Figure 8: M. Tanabe et al., submitted to High Energy Density Physics

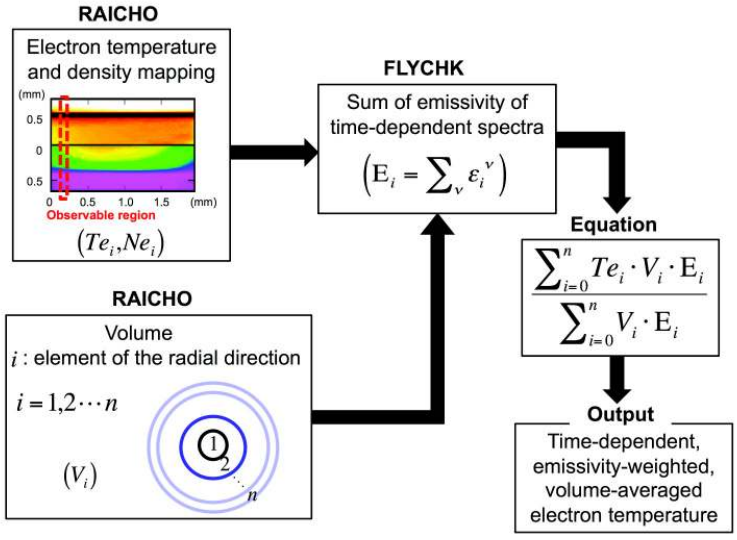

Figure 9: M. Tanabe et al., submitted to High Energy Density Physics

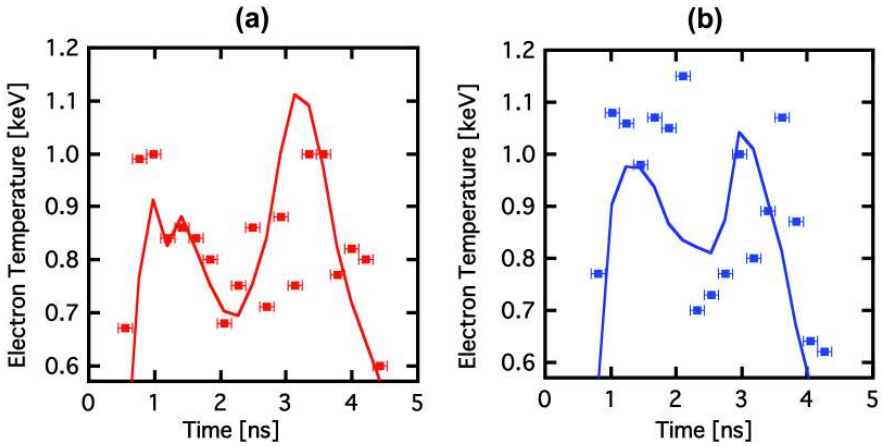

Figure 10: M. Tanabe et al., submitted to High Energy Density Physics